The Astrophysical Journal, 880:2 (14pp), 2019 July 20 https://doi.org/10.3847/1538-4357/ab2717

Spatially Resolved Interstellar Medium and Highly Excited Dense Molecular Gas in the Most Luminous Quasar at $z = 6.327$

Feige Wang[1,2], Ran Wang[2], Xiaohui Fan[3], Xue-Bing Wu[2,4], Jinyi Yang[3], Roberto Neri[5], and Minghao Yue[3]
[1] Department of Physics, University of California, Santa Barbara, CA 93106-9530, USA; fgwang@physics.ucsb.edu
[2] Kavli Institute for Astronomy and Astrophysics, Peking University, Beijing 100871, People's Republic of China
[3] Steward Observatory, University of Arizona, 933 North Cherry Avenue, Tucson, AZ 85721, USA
[4] Department of Astronomy, School of Physics, Peking University, Beijing 100871, People's Republic of China
[5] Institute de Radioastronomie Millimetrique, St. Martin d'Heres, F-38406, France
Received 2018 December 2; revised 2019 May 30; accepted 2019 June 3; published 2019 July 17

Abstract

Among more than 200 quasars known at $z \gtrsim 6$, only one object, J0100+2802 ($z = 6.327$), was found hosting a $>10^{10}\,M_{\odot}$ supermassive black hole. In order to investigate the host galaxy properties of J0100+2802, we performed multi-band ALMA observations, aiming at mapping the dust continuum, [C II] and CO(6–5) emission lines with subkiloparsec scale resolution, as well as detecting high-J CO lines in CO(11–10), CO(10–9), and CO(7–6). The galaxy size is measured to be $R_{\rm major} = 3.6 \pm 0.2$ kpc from the high-resolution continuum observations. No ordered motion on kiloparsec scales was found in either the [C II] or the CO(6–5) emission. The velocity dispersion is measured to be $161 \pm 7\,{\rm km\,s^{-1}}$, which is about three times smaller than that estimated from the local M–σ relation. In addition, we found that the CO emission is more concentrated (a factor of 1.8 ± 0.4) than the [C II] emission. Together with CO(2–1) detected by the Very Large Array (VLA), we measured the CO spectral line energy distribution, which is best fit by a two-component model that includes a cool component at ∼24 K with a density of $n_{(\rm H_2)} = 10^{4.5}\,{\rm cm^{-3}}$, and a warm component at ∼224 K with a density of $n_{(\rm H_2)} = 10^{3.6}\,{\rm cm^{-3}}$. We also fit the dust continuum with a graybody model. This indicated that the continuum has either a high dust emissivity $\beta \gtrsim 2$ or a hot dust temperature $T_{\rm dust} \gtrsim 60$ K, or a combination of these two factors. The highly excited CO emission and hot dust temperature suggest that the powerful active galactic nucleus in J0100+2802 could contribute to the gas and dust heating, but future observations are needed to confirm this.

Key words: cosmology: observations – early universe – galaxies: active – galaxies: high-redshift – quasars: individual (J0100+2802)

1. Introduction

In the past decade, the advent of wide-area optical and infrared surveys has resulted in the discovery of more than 200 luminous quasars at $z \sim 6$ (e.g., Fan et al. 2001; Jiang et al. 2008; Willott et al. 2010; Mortlock et al. 2011; Bañados et al. 2016; Wang et al. 2017, 2018b; Matsuoka et al. 2018; Yang et al. 2019) with the highest redshift at $z = 7.5$ (Bañados et al. 2018). These quasars are powered by $\sim 10^9\,M_{\odot}$ supermassive black holes (SMBHs; e.g., Jiang et al. 2007; Shen et al. 2019). The discovery of a $1.24 \times 10^{10}\,M_{\odot}$ BH at $z = 6.3$ (Wu et al. 2015) and $\sim 10^9\,M_{\odot}$ BHs at $z > 7$ (Mortlock et al. 2011; Bañados et al. 2018; Wang et al. 2018a; Yang et al. 2019) challenges theories of the formation and growth of SMBHs in the early universe (e.g., Pacucci et al. 2015).

Deep imaging of quasar host galaxies allows studies of how mergers and star formation activities affect the central nuclei, and vice versa. However, the nuclear region of a quasar is extremely bright in the rest-frame ultraviolet (UV), which prevents direct detections of the host galaxies and galactic environments of luminous quasars with ground-based telescope. Mechtley et al. (2012) obtained deep near-infrared *Hubble Space Telescope* Wide Field Camera 3 images of the $z = 6.42$ quasar J1148+5251. However, even with careful point-spread function (PSF) subtraction, only an upper limit of UV emissions from the host galaxy is measured. Such observations indicate an infrared excess of $\log({\rm IRX}) > 1.0$ in the host galaxies of luminous quasars at the end of reionization, comparable to that of the most luminous infrared galaxies in the local universe.

On the other hand, submillimeter and millimeter observations of both the dust continuum [C II] 158 μm fine-structure lines and molecular CO lines of high-redshift quasar host galaxies directly probe the star formation and interstellar medium properties of the quasar hosts. This provides the most useful observational probe of the growth of massive galaxies and the relation between SMBHs and their hosts in early epochs (see Carilli & Walter 2013; Gallerani et al. 2017, and references therein). The recent [C II] survey of ∼30 $z \gtrsim 6$ quasars with the Atacama Large Millimeter Array (ALMA) shows that the SMBH-host galaxy mass ratio on average is about one dex above the local value (Decarli et al. 2018), and that there is no correlation between the black hole (BH) accretion measured from UV luminosity and stellar mass and star formation inferred from far-infrared (FIR) luminosity (Venemans et al. 2018). These findings suggest that BHs in the most luminous quasars at the end of reionization might not coevolve with their host galaxies, in the sense that they do not follow the same relation between the mass of SMBHs and the bulge masses of their host galaxies as established in the local universe.

The ultraluminous quasar, SDSS J010013.02+280225.8 (hereafter, J0100+2802) at $z = 6.3$, with a bolometric luminosity of $4.29 \times 10^{14}\,L_{\odot}$ and a $1.24 \times 10^{10}\,M_{\odot}$ SMBH, is by far the most optically luminous quasar with the most massive SMBH known at $z > 6$. J0100+2802 was discovered by Wu et al. (2015) using the optical plus mid-infrared color selection developed by Wang et al. (2016). The sphere of influence ($r_{\rm SOI} = {\rm GM_{BH}}/\sigma^2$) of this massive SMBH is at

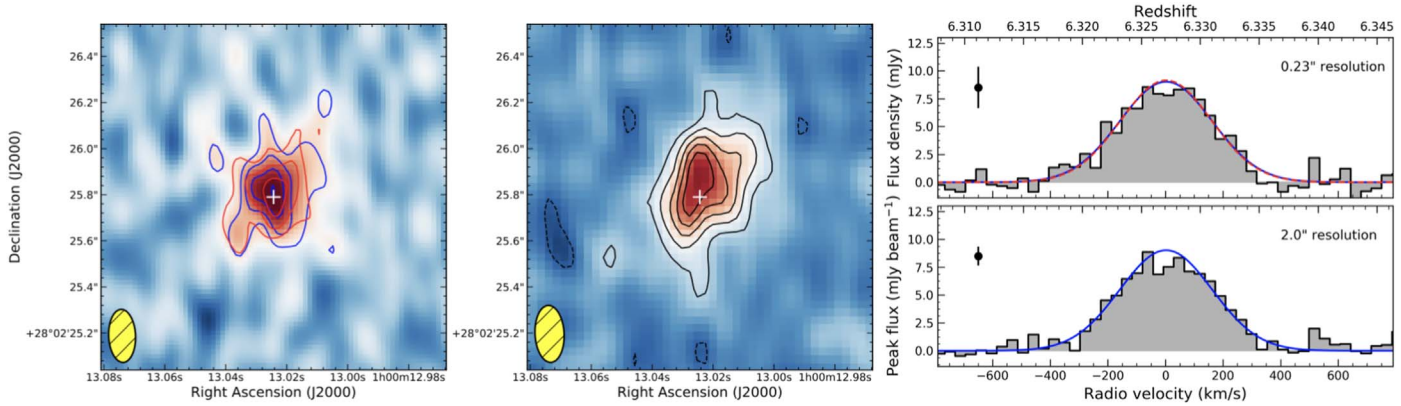

Figure 1. Left: continuum-subtracted map of [C II] emission. The blue and red sides of the emission line are shown in blue and red contours, respectively. The blue side emission is averaged over from −300 to −150 km s^{-1}, and the red side emission is averaged over from +150 to +300 km s^{-1}. Contour levels are +3σ, +4σ, +5σ, and +6σ. The ALMA beam is shown in the bottom left corner, which is 0.″23 × 0.″12. The white signs in all maps in this paper indicate the optical position of the quasar obtained from GAIA. Middle: map of 251 GHz continuum emission. Contour levels are −2σ, +3σ, +5σ, +7σ, +9σ, and +11σ, with $\sigma \sim 17$ μJy. The beam size is 0.″25 × 0.″13. Bottom right: spectrum extracted from the peak pixel in the tapered [C II] cube. The solid blue line denotes the Gaussian fit. Top right: spectrum extracted from the full-resolution [C II] map with an extraction aperture radius of 0.″67. The red dashed line is the Gaussian fit to this spectrum, and the blue solid line is the Gaussian fit to the spectrum shown in the top panel. The bins are 31.25 MHz wide, which corresponds to ∼36 km s^{-1}. The typical 1σ uncertainties per 31.25 MHz bin are 0.85 mJy beam^{-1} and 0.21 mJy beam^{-1} for the tapered [C II] cube and the full-resolution [C II] cube. The uncertainty shown in the top panel is the 1σ flux density uncertainty within the extraction region per 31.25 MHz, which is 1.86 mJy.

subkiloparsec (subkpc) scale, which could be resolved by ALMA. Thus, J0100+2802 is a unique source for studying the relation between BH growth and galaxy assembly in the early universe.

In Wang et al. (2016), we detected [C II], CO(6–5) and CO(2–1) emissions in the host galaxy of J0100+2802. Our observations indicated that J0100+2802 only has moderate FIR emission, and the narrow emission line width suggests that it is likely to be well above the local M–σ relation. However, large uncertainties remain in determining the properties of the host galaxy of J0100+2802, limited by the low spatial resolution (∼2.″0 or ∼10 kpc at the quasar redshift) and small number of CO lines detected. In this paper, we present ALMA imaging in [C II] and CO(6–5) lines with subkpc spatial resolution. We also report the detection of multiple high-J CO lines with ALMA observations. The [C II] observations were performed in ALMA Cycle 3 and the CO line observations were obtained in Cycle 5. The paper is organized as follows: In Section 2 we describe our new ALMA observations of J0100+2802 and basic measurements based on these observations. In Section 3 we describe its dust properties (including dust temperature, emissivity index, and dust mass), FIR luminosity, and star formation rate (SFR). In Section 4 we present constraints on its gas excitations from the spectral line energy distribution (SLED) of the CO emission lines and fine-structure line ratios. In Section 5 we discuss the gas kinematics, dynamical mass measurements, and mass budget in J0100+2802. We also briefly discuss the sphere of influence of the central SMBH. We summarize our findings in Section 6. Throughout the paper, we adopt a ΛCDM cosmological model with parameters $\Omega_\Lambda = 0.7$, $\Omega_m = 0.3$, and $H_0 = 70$ km s^{-1} Mpc^{-1}.

2. Observations and Measurements

2.1. [C II] Fine-structure Line Observations

At $z = 6.32$, the [C II] emission line is redshifted from 1901 to 259 GHz. We observed the [C II] emission of J0100+2802 in ALMA band 6 with the C36-6 configuration on 2016 September 4. The total on-source time was 74 minutes. We tuned the receivers to cover the redshifted [C II] line in spectral window 1 and to cover the continuum with the other three spectral windows. Bandpass calibration was performed through observations of J0237+2848, and J2253+1608. For the flux and amplitude calibration, the sources J0238+1636 and J2253+1608 were observed. The source J0057+3021 was observed as phase calibrator.

The data were reduced using the Common Astronomy Software Application (CASA; McMullin et al. 2007), following standard reduction steps. We first subtracted the underlying continuum of [C II] by fitting a UV-plane model with the *uvcontsub* task. We then imaged the line data cube using the *tclean* task with Briggs weighting and a robustness parameter of 0.5, which optimizes the noise per frequency bin and the resolution of the resulting map. The synthesized beam size at the frequency of [C II] is 0.″23 × 0.″12. The 1σ root mean square (rms) sensitivity is 0.21 mJy/beam per ∼36 km s^{-1} channel.

We use the data cube of [C II] over the velocity range from −300 to 300 km s^{-1} to derive the intensity map of [C II] emission. Similarly, the intensity map for all other lines described in the following sections are also derived with the same parameters. The [C II] emission line in J0100+2802 is clearly detected in the continuum-subtracted [C II] map (Figure 1). The underlying continuum map is also shown in Figure 1. We fit the velocity-integrated [C II] emission intensity map with *imfit* and derive the image component size to be 0.″47 × 0.″39, which is more than twice larger than the beam size in the major and minor axis direction. We measure a deconvolved image size of (0.″43 ± 0.″10) × (0.″34 ± 0.″09). Throughout this paper the sizes are quoted as FWHM size and the errors are estimated from the *imfit* fitting of elliptical Gaussians based on the work of Condon (1997) unless indicated otherwise. The line flux measured from 2D Gaussian fitting on the intensity map is 3.04 ± 0.48 Jy km s^{-1}. Our deep ALMA imaging with subkpc scale (1.27 × 0.67 kpc^2) resolution has resolved the [C II] emission of J0100+2802 well. One way to determine whether the size measured from the image plane is affected by the "missing" flux is to fit the *uv* data directly (e.g., Ikarashi et al. 2015; Hodge et al. 2016). We fit

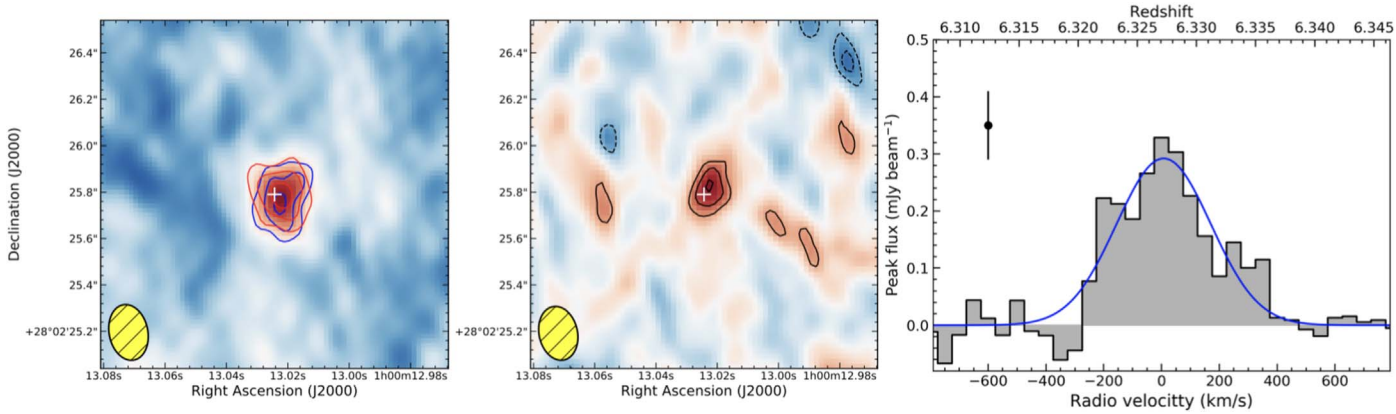

Figure 2. Left: continuum-subtracted high spatial resolution map of CO(6–5) emission. The blue and red sides of the emission line are shown in cyan and red contours, respectively. The blue side emission is averaged over from -300 km s^{-1} to -150 km s^{-1}, and the red side emission is averaged over from $+150$ km s^{-1} to $+300$ km s^{-1}. Contour levels are $+3\sigma$, and $+4\sigma$. The beam is shown in the bottom left corner, which is $0\farcs24 \times 0\farcs17$. Middle: high-resolution map of the 99.4 GHz continuum emission. Contour levels are -3σ, -2σ, $+2\sigma$, $+3\sigma$, and $+4\sigma$, with $\sigma \sim 6$ μJy. The beam with a size of $0\farcs24 \times 0\farcs17$ is plotted in the bottom left corner. Right: spectrum extracted from the peak pixel in the CO(6–5) data cube. The solid blue line denotes the Gaussian fit. The bins are 60 km s^{-1} wide. The uncertainty shown in the plot is 1σ in flux density per 60 km s^{-1} bin width, which is 0.06 mJy beam^{-1}.

the *uv*-data with the *uvmodelfit* routine in CASA by assuming an elliptical Gaussian profile. In the fitting, we only select visibility from the continuum-subtracted data with frequency between 250 GHz and 250.8 GHz to ensure that we measure the size of the [C II] emission. The best-fit *uv*-model of the [C II] emission gives a size of $(0\farcs49 \pm 0\farcs06) \times (0\farcs39 \pm 0\farcs05)$ or $(2.72 \pm 0.33) \times (2.16 \pm 0.28)$ kpc^2, which agrees with (within the uncertainties) that derived from the fitting in the image plane, suggesting that the sizes measured in the image plane are robust, and that they are not significantly affected by the presence of potentially "missing" emission.

To account for spatially extended low-level [C II] emission and measure the total flux for [C II], we tapered the [C II] map by setting *uvtaper* $= 1\farcs5$ in the *tclean* task. The tapered cube has a beam size of $2\farcs01 \times 1\farcs53$, comparable with our previous Plateau de Bure Interferometer (PdBI) observation (Wang et al. 2016). Figure 1 shows the spectra extracted from both the tapered and the full-resolution [C II] map and the Gaussian fits. The spectrum extracted from the tapered map uses the peak pixel in the cube, and the spectrum extracted from the full-resolution cube uses the flux densities within an aperture radius of $0\farcs67$ centered at the center position of the velocity-integrated [C II] map. The extraction aperture is determined by matching the [C II] line flux to that of the tapered image.

The redshifts measured from both spectra are 6.3270 ± 0.0005. We refer to $z = 6.327$ as the systemic redshift of J0100+2802 throughout the paper. The FWHM of the [C II] line is measured to be 380 ± 16 km s^{-1} from the tapered spectrum, and 373 ± 25 km s^{-1} from the full-resolution spectrum. The total [C II] line flux is measured to be 3.64 ± 0.22 Jy km s^{-1} with a single-Gaussian fitting to the spectrum extracted from the tapered cube. This is consistent with the flux (3.36 ± 0.46 Jy km s^{-1}) measured from our previous PdBI observations (Wang et al. 2016). The line flux measured from the 2D Gaussian fitting on the intensity map is lower than that measured from the tapered spectrum, which also supports that extended emission exists beyond the bright core.

In Figure 1 we also overplot the contours of the [C II] intensity from the blue and red sides of the emission line, which are derived by integrating blue side emissions from -300 km s^{-1} to -150 km s^{-1} and integrating red side emissions from $+150$ km s^{-1} to $+300$ km s^{-1}, respectively. The peak positions of the blue and red side emissions coincide with that of the entire [C II] intensity map and quasar optical position, which suggests that the [C II] emission traced gas does not show ordered motions on scales of $\sim$1 kpc.

2.2. CO Molecular Line Observations

We observed CO(6–5) in ALMA band 3 with the C43-7 configuration to reach a similar spatial resolution with that of the [C II] observations. The data were taken from 2017 November 18 to November 20 with a total on-source time of 141 minutes. Bandpass calibration was performed through observations of J0238+1636 and J2253+1608. For the flux and amplitude calibration, the sources J0238+1636, and J2253 +1608 were observed. As with the [C II] observations, the source J0057+3021 served as phase calibrator. The data were processed using a similar strategy as for [C II] observations. The main difference was that we imaged the CO line data cubes using a weighting factor of robust $= 2$ (i.e., natural weight scheme) to maximize the signal-to-noise ratio. The synthesized beam size at the frequency of CO(6–5) is $0\farcs24 \times 0\farcs17$.

We fit the CO(6–5) intensity map (Figure 2) with *imfit*. The fitting gives an image size (convolved with the beam) of $0\farcs34 \times 0\farcs27$, which is slightly larger than the beam size ($0\farcs24 \times 0\farcs17$). This suggests that we marginally resolved the CO(6–5) emission at the designed resolution. The deconvolved size of CO(6–5) is $(0\farcs26 \pm 0.09) \times (0\farcs19 \pm 0.11)$, or $(1.44 \pm 0.50) \times (1.05 \pm 0.61)$ kpc^2. As indicated in Section 2.1, the size measured from the image plane is robust, and the CO(6–5) emission is also only marginally resolved and thus less affected by possible "missing" fluxes. We adapt the size measured from *imfit* as the size of CO(6–5) emission. The size (major axes) of the CO(6–5) emission is 1.8 ± 0.4 times smaller than that of the [C II] emission, indicating that the molecular gas is more centrally concentrated than [C II]. A similar result is also reported in the host galaxy of a bright $z = 6$ quasar (Feruglio et al. 2018).

We also extract the spectrum at the peak pixels in the CO(6–5) data cube, shown in Figure 2. We fit the extracted spectrum with a single-Gaussian function, which yields a

redshift of 6.3271 ± 0.0006, an FWHM of 383 ± 32 km s^{-1}, and a line flux of 0.11 ± 0.02 Jy km s^{-1}. Both redshift and line widths of CO(6–5) lines are well consistent with that of the [C II] emission line. The line flux estimated from the extracted spectrum at the peak position is about three times lower than that from the 2D Gaussian fitting of the CO(6–5) intensity map. This agrees with the argument that we marginally resolved the CO(6–5) emission; a disparity like this between line fluxes measured from fitting extracted spectrum and 2D map is often seen in the marginally resolved observations of [C II] emission lines (e.g., Decarli et al. 2018, see their Figure 6). In order to measure the total line flux, we tapered the CO(6–5) data cube with *uvtaper* = 1.″5. We found a line flux of 0.26 ± 0.05 Jy km s^{-1} at the peak position, which is consistent with that measured in our low-resolution PdBI observations (Wang et al. 2016).

Following the analysis performed on the [C II] emission, we derive the blue and red intensity maps by integrating the blue side emissions from −300 to −150 km s^{-1} and the red side emissions from +150 to +300 km s^{-1}. There is no measurable offset between the blue and red side emissions of the CO(6–5) line considering the beam size and the low detection significance of the blue and red side emissions (Figure 2), which suggests that CO(6–5) also does not show ordered motions on scales of ∼1 kpc.

We also observed CO(7–6) in ALMA band 3 with the C43-5 configuration, CO(10–9) in ALMA band 4 with the C43-4 configuration, and CO(11–10) in ALMA band 5 with the C43-5 configuration. The data were taken on 2017 December 25 with 49 minutes on-source exposure for CO(7–6), on 2018 January 15 with 49 minutes on-source exposure for CO(10–9), and on 2018 September 18 with 61 minutes on-source exposure for CO(11–10). Bandpass calibration was performed through observations of J0237+2848, J0238+1636, and J2253+1608. For the flux and amplitude calibration, the sources J0237+2848, J0238+1636, and J2253+1608 were observed. The source J0057+3021 served as phase calibrator for all CO observations. We tuned one spectral window centered at the expected frequency of each line and the other three spectral windows for the continuum. The synthesized beam sizes at the frequency of CO(7–6), CO(10–9) and CO(11–10) are 0.″60 × 0.″42, 0.″73 × 0.″49, and 0.″60 × 0.″45, respectively.

The velocity-integrated intensity maps of CO(11–10), CO(10–9), and CO(7–6) are shown in Figure 3. CO(11–10) is detected at the 7σ level with a line flux of 0.28 ± 0.04 Jy km s^{-1} at the peak position. We also use *imfit* to fit the line emission, which gives a line flux of 0.30 ± 0.04 Jy km s^{-1}, consistent with the peak line flux. The CO(10–9) and CO(7–6) emissions are marginally detected in the velocity-integrated intensity map. We thus adapt the line fluxes at the peak positions of these two CO lines as their brightness. The line fluxes are 0.25 ± 0.05 Jy km s^{-1} and 0.22 ± 0.06 Jy km s^{-1} for CO(10–9) and CO(7–6), respectively. To be consistent with other CO line flux measurements, we also use the line flux (0.28 ± 0.04 Jy km s^{-1}) at the peak position for CO(11–10) in the following sections. We also search for the [C I](2–1) 370 μm emission line (close to CO(7–6) emission) in the CO(7–6) data cube. We integrate the data over the velocity range from −300 to 300 km s^{-1}. This yields a 3σ upper limit for the line flux of 0.18 Jy km s^{-1}. The line maps, underlying continuum maps, and the extracted spectra for these three CO lines are shown in Figure 3. The line fluxes and luminosities of all emission lines are listed in Table 1.

2.3. Dust Continuum Emissions

The line emission observations are also used to measure the underlying dust continuum emissions as shown in Figure 1 through Figure 3. Our observations at the [C II] setup provide continuum observations with the highest signal-to-noise ratio. In order to cover more frequency space, we generate three continuum maps from the [C II] observations. One is created by averaging the line-free channels in the upper side band. This map provides the measurements of the continuum flux density at the mean frequency of 258 GHz. The second map is constructed by averaging all the channels in the spectral windows in the lower side band, which provides the measurements of the continuum flux density at the mean frequency of 244 GHz. The third map is constructed by averaging all line-free channels, including the lower and upper side band. This map is centered at 251 GHz and provides the most sensitive measurement of the dust continuum. The final continuum 1σ rms sensitivities at 258 GHz, 251 GHz, and 244 GHz are 25 μJy/beam, 17 μJy/beam, 21 μJy/beam, respectively. The 251 GHz continuum map that has the highest signal-to-noise ratio is shown in Figure 1.

In order to measure the sizes of the dust-emitting regions, we fit 2D Gaussian functions to the three continuum maps close to [C II] using the *imfit* routine. We derive a deconvolved size of (0.″47 ± 0.″06) × (0.″27 ± 0.″04) and an integrated continuum flux density of 1.04 ± 0.10 mJy for the deepest 251 GHz continuum map. The sizes of the 258 and 244 GHz continuum emissions are measured to be (0.″46 ± 0.″08) × (0.″25 ± 0.″06), and (0.″48 ± 0.″08) × (0.″27 ± 0.″05), respectively. The integrated continuum flux densities at 258 and 244 GHz are 1.08 ± 0.15 mJy and 0.98 ± 0.13 mJy, respectively.

The continuum flux density measured around [C II] emission is only ∼80% of that measured from an unresolved (beam size is 2.″0 × 1.″7) PdBI observation (Wang et al. 2016), which suggests that the continuum emission is well resolved. In order to measure the total continuum flux density (i.e., including faint extended emissions), we taper the continuum map with *uvtaper* = 1.″5 in the *tclean* task. The peak flux densities measured from the tapered image are 1.47 ± 0.10 mJy beam^{-1}, 1.26 ± 0.08 mJy beam^{-1} and 1.11 ± 0.09 mJy beam^{-1} for 258 GHz, 251 GHz, and 244 GHz, respectively. To measure the size of the missing extended continuum emission, we perform aperture photometry on the most sensitive continuum map at 251 GHz. We measure flux densities with a range of apertures, and the growth curve is shown in the left panel of Figure 4. The curve is flat at radius $\gtrsim$0.″68 with a flux density consistent with the value observed at lower resolution (Wang et al. 2016).

We also fit the *uv*-data of our band-6 continuum observations with the *uvmodelfit* task by assuming an elliptical Gaussian profile. The right panel of Figure 4 shows the *uv* data and the best-fit *uv*-model profiles of the visibility, which have been radially averaged in bins of 40 kλ. The best-fit *uv*-model gives a total flux of 1.23 ± 0.05 mJy and a size of (0.″51 ± 0.″03) × (0.″31 ± 0.″02) or (2.83 ± 0.11) × (1.72 ± 0.11) kpc^2 at 251 GHz. The flux is well consistent with what is measured from the tapered 251 GHz continuum image, and the size is slightly larger than

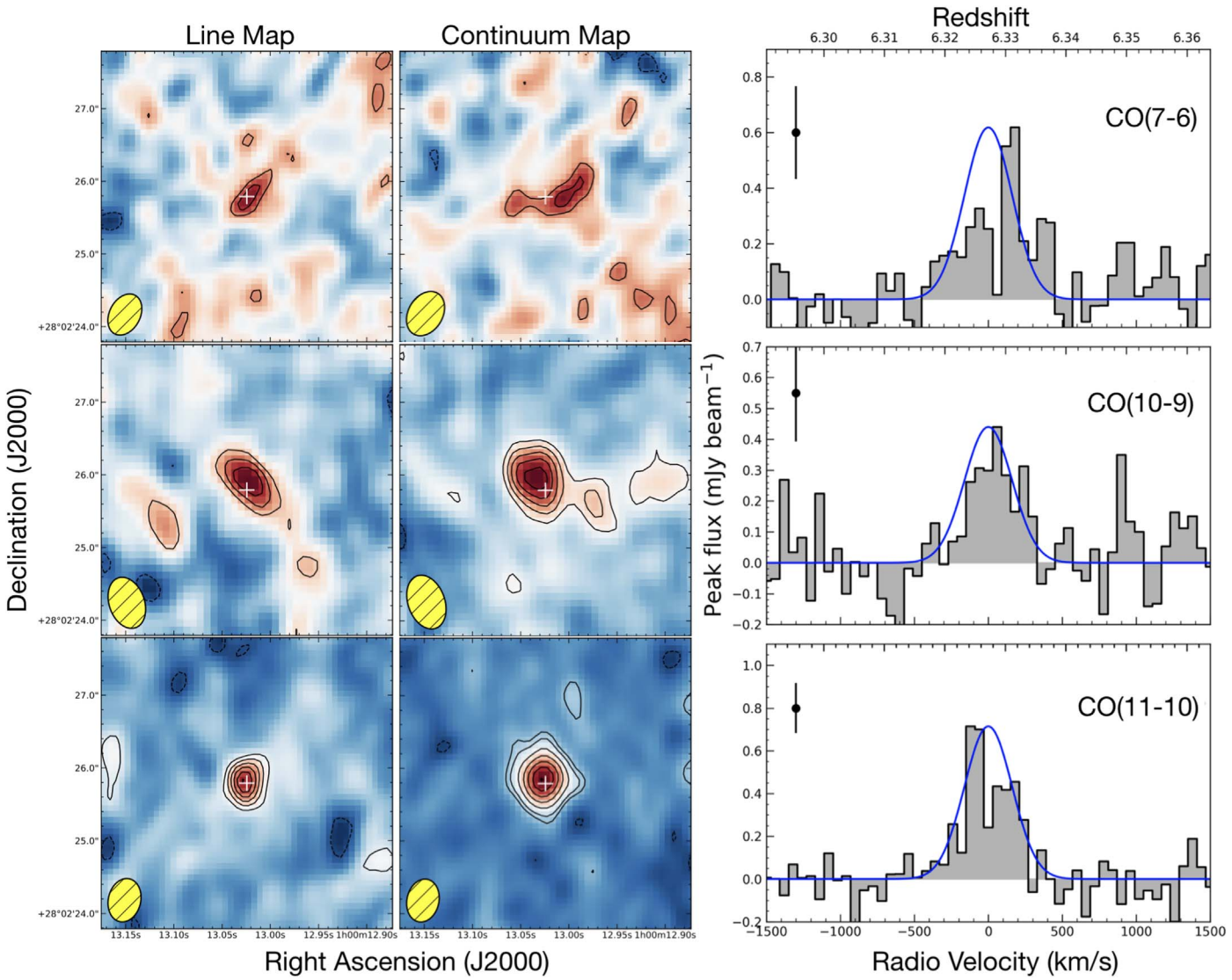

Figure 3. Low spatial resolution CO and underlying continua observations. The left column shows the CO(7–6), CO(10–9), and CO(11–10) continuum-subtracted line emission maps from top to bottom. The contours start from $+2\sigma$ increasing by σ, with $\sigma \sim 0.06$ Jy km s^{-1} beam^{-1}, $\sim$0.05 Jy km s^{-1} beam^{-1}, and $\sim$0.04 Jy km s^{-1} beam^{-1} for the CO(7–6), CO(10–9), and CO(11–10) line maps, respectively. The -2σ contours are shown as dashed lines. The beams are shown as yellow ellipticals. The middle column shows the 103 GHz, 152 GHz, and 180 GHz continuum emissions from top to bottom. The contour levels for the 103 GHz continuum are -2σ, $+2\sigma$, and $+3\sigma$, with $\sigma \sim 12$ μJy beam^{-1}. The contour levels for the 152 GHz continuum are -2σ, $+2\sigma$, $+3\sigma$, $+4\sigma$, $+5\sigma$, and $+6\sigma$, with $\sigma \sim 17$ μJy beam^{-1}. The contour levels for the 180 GHz continuum are -2σ, $+2\sigma$, $+3\sigma$, $+5\sigma$, $+7\sigma$, $+9\sigma$, $+11\sigma$, and $+13\sigma$, with $\sigma \sim 19$ μJy beam^{-1}. The right column shows the spectra for the CO(7–6), CO(10–9), and CO(11–10) lines from top to bottom. The blue curves are Gaussian profiles with amplitudes equal to the maximum peak flux densities of each line and FWHM = 380 km s^{-1} centered at the [C II] based redshift. The line fluxes derived from Gaussian profiles are 0.25 Jy km s^{-1}, 0.18 Jy km s^{-1}, and 0.29 Jy km s^{-1} for CO(7–6), CO(10–9), and CO(11–10), respectively.

that measured from the high-resolution continuum image. We define the radius of the quasar host galaxy, $R_{\rm major}$, as the position where it is 3σ (i.e., containing 99.7% information) away from the line center along the major axis. Based on the best-fit *uv*-model, we measure $R_{\rm major} = 0\farcs65 \pm 0\farcs04$ or $R_{\rm major} = 3.6 \pm 0.2$ kpc, which is consistent with both the growth curve measured from the continuum image and the size of the [C II] emission region. Because the 251 GHz has the highest sensitivity of our observations, we use the $R_{\rm major}$ derived here to constrain the dynamical mass of the quasar host galaxy in Section 5.2.

We also generate continuum maps from each CO line observation by averaging line-free regions in all four spectral windows. The final continuum 1σ rms sensitivities at 99 GHz, 103 GHz, 152 GHz and 180 GHz are 4.3 μJy/beam, 12 μJy/beam, 17 μJy/beam, and 19 μJy/beam, respectively. The high-resolution continuum map at 99 GHz is shown in Figure 2, and other continuum maps with relative lower resolutions are shown in Figure 3.

We fit the continuum map around CO(6–5) with *imfit*. The image size (convolved with the beam) is $0\farcs28 \times 0\farcs16$, comparable to the beam size ($0\farcs24 \times 0\farcs17$), which suggests that the continuum emission at 99 GHz (at least the bright core) is unresolved. The peak flux density is measured to be 25 ± 6 μJy. We also tapered the continuum image at 99 GHz with *uvtaper* = $1\farcs5$, which gives a flux density at the peak position of 36 ± 17 μJy. The peak flux density from the tapered image is about 1.4 times higher than that from the full-resolution map, which suggests that we may have missed some extended faint emissions in the high-resolution map. Thus, we

Table 1
Line Properties of J0100+2802

	[C II]	[C I][a]	CO(11–10)	CO(10–9)	CO(7–6)	CO(6–5)	CO(2–1)[b]
Line Flux (Jy km s^{-1})	3.64 ± 0.22	<0.18	0.28 ± 0.04	0.25 ± 0.05	0.22 ± 0.06	0.26 ± 0.05	0.038 ± 0.013
Line Luminosity (10^8 $L_\odot$)	37.02 ± 2.24	<0.78	1.90 ± 0.27	1.54 ± 0.31	0.95 ± 0.26	0.96 ± 0.19	0.05 ± 0.02
Line Luminosity (10^{10} K km s^{-1} pc^2)	1.69 ± 0.10	<0.46	0.29 ± 0.04	0.32 ± 0.06	0.57 ± 0.15	0.91 ± 0.17	1.20 ± 0.41

Notes.
[a] 3σ limits.
[b] Line flux is measured from the NSF Karl G. Jansky Very Large Array (VLA) by Wang et al. (2016).

choose the peak flux density measured from the tapered image as the brightness at 99 GHz.

The continuum at 103 GHz is only marginally detected. Therefore, instead of fitting the 2D continuum map, we adapt the peak flux density as the brightness, which is 43 ± 12 μJy. The continuum emission at 152 GHz is detected at $>6\sigma$, and we measure the flux density to be 178 ± 19 μJy for the bright core with *imfit*. We measure the continuum flux at 180 GHz to be 362 ± 35 μJy by using *imfit*. The continuum emissions at 103 GHz, 152 GHz, and 180 GHz are not resolved (i.e., the major axis of object is $<1.2\times$ that of beam) at the designed resolution. All continuum flux density measurements are listed in Table 2.

J0100+2802 is the only quasar at $z > 5.5$ that is detected by *GAIA* and thus provides us the opportunity to investigate whether the position of the rest-frame UV AGN emission is offset from the (sub-) millimeter emissions. In Figures 1 to 3 we overplot the optical position measured from *GAIA*. The *GAIA* position is fully consistent with the (sub-) millimeter emissions in both continuum and [C II] with no measurable offsets.

3. Dust Emission Properties

3.1. Dust Temperature and Emissivity Index

Most high-redshift quasars lack full FIR spectral energy distribution (SED) measurements, and $L_{\rm FIR}$ and $M_{\rm dust}$ are commonly determined with single or two photometric measurements by assuming an optically thin graybody model with a dust temperature of $T_{\rm dust} = 47$ K and an emissivity index of $\beta = 1.6$ (e.g., Wang et al. 2016; Venemans et al. 2018). This temperature and emissivity index are measured from fitting a combined SED of a sample of high-redshift quasars with two or more rest-frame FIR photometric measurements by Beelen et al. (2006). However, both parameters have large scatters in different systems (e.g., Priddey & McMahon 2001; Leipski et al. 2013). In this section, we combine the continuum measurements from Wang et al. (2016) and Wang et al. (2017) with our new ALMA observations to constrain the dust emission properties in J0100+2802. Before fitting the dust continuum, we subtract the radio emissions determined by the 3 and 32 GHz emission with the form of $f_\nu \propto \nu^{-0.9}$ (Wang et al. 2016). Note that the VLBA 1.5 GHz observation does not follow the steep spectra determined from the 3 GHz and 32 GHz observations, which could be caused by the change in spectral slope or the fact that the very high resolution VLBA observations could have missed some extended flux, as discussed in Wang et al. (2017).

As suggested by previous works (e.g., da Cunha et al. 2013; Venemans et al. 2016, 2017a), it is important to take the effects of the cosmic microwave background (CMB) into account when studying high-redshift objects. The CMB temperature at $z = 6.3$ ($T_{\rm CMB} \sim 20$ K) is only slightly lower than dust temperatures in high-redshift quasar hosts, which reduces the flux densities that we can measure from sources at such high redshifts. We take the CMB effects into account following da Cunha et al. (2013), who introduced a correction factor as a function of frequency and dust temperature at a certain redshift.

Note, however, that most of the continuum points are on the Rayleigh–Jeans tail of the dust emission, and we cannot tightly constrain the temperature and emissivity at the same time. Figure 5 shows the FIR dust continuum of the J0100+2802 host as well as different dust emission models with a set of β and $T_{\rm dust}$ after taking into account the effects of the CMB as discussed above. We test a series of different graybody models. The different sets of graybody models as well as the radio continuum emission are shown in Figure 5. First, we set both dust emissivity index β and dust temperature $T_{\rm dust}$ as free parameters, which yields $\beta = 2.28 \pm 0.26$ and $T_{\rm dust} = 86 \pm 54$ K (gray solid line in Figure 5).

Because we do not have any continuum measurements at shorter wavelength, $T_{\rm dust}$ has a large uncertainty. We then fix the temperature to be $T_{\rm dust} = 47$ K and vary β in the fitting, which gives $\beta = 2.64 \pm 0.07$ (magenta solid line in Figure 5). The emissivity index is higher than the expected $\beta = 2$ for pure silicate and/or graphite grains (e.g., Draine & Lee 1984). However, a high emissivity index like this is also found in some local ultraluminous infrared galaxies (ULIRGs) and can be explained by the presence of more than one single dust component (e.g., Clements et al. 2010).

In order to better understand the allowed dust temperature and emissivity index in the host galaxy of J0100+2802, we further explore two different sets of graybody models in which β is held fixed ($\beta = 1.6$ and $\beta = 1.95$), while the temperature is varied. These models are overplotted in Figure 5. By comparing these different models, we find that with slightly higher temperatures, models with β fixed to 1.6 ($T_{\rm dust} \gtrsim 80$ K) and 1.95 ($T_{\rm dust} \gtrsim 60$ K) can also fit the data reasonably well. The upper limit from the 450 μm observation suggests, however, that the dust temperature should not be higher than ~100 K. The degeneracy between high β and warm $T_{\rm dust}$ could be solved with ALMA band 9 and band 10 observations that reach the peak frequency of the SED.

Because we only have rest-frame FIR continuum detections, we cannot perform a multicomponent fitting as investigated by Leipski et al. (2013). In order to further probe whether the temperature and emissivity index derived above are affected by different fitting methods, we directly compare the observed continuum flux ratios of J0100+2802 with other luminous $z \gtrsim 6$ quasars (i.e., model-free comparison). As most previous continuum observations of $z \gtrsim 6$ quasars are mainly focused on frequencies close to the [C II] and CO(6–5) lines, we derived

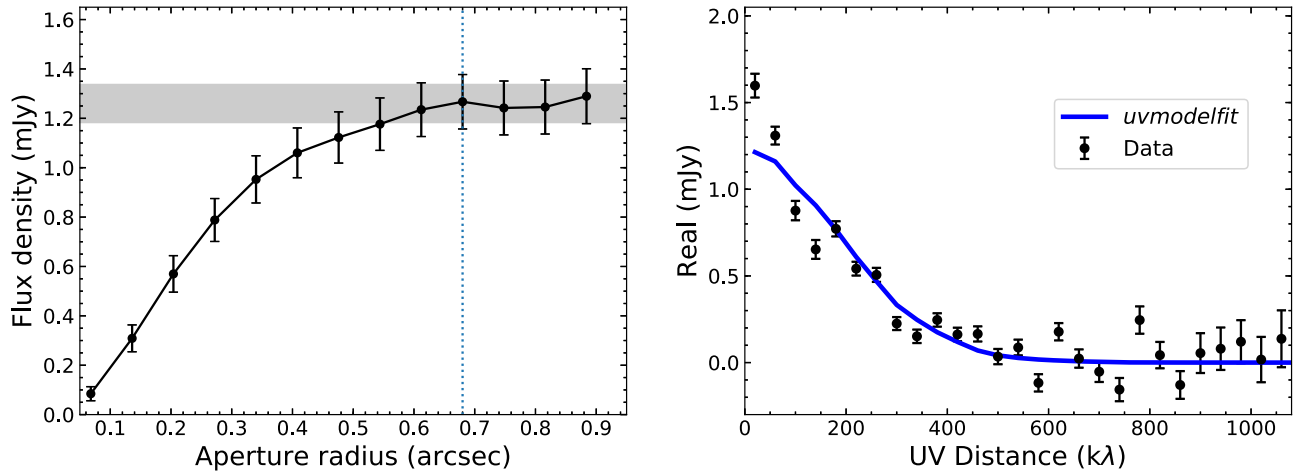

Figure 4. Left: the flux density of the 251 GHz continuum emission as a function of aperture radius. The flux density reaches a roughly constant value at radius $\gtrsim 0\farcs68$. This is consistent with the peak flux density (gray shaded region) measured from the tapered continuum map. Right: visibility (*uv*-) profile of the continuum emission from our band-6 observations. The visibility is radially averaged with a bin size of 40 kλ (black points). The blue solid line is the best-fit *uv* model, which gives a size of FWHM = $(0\farcs51 \pm 0\farcs02) \times (0\farcs31 \pm 0\farcs02)$ and a flux density of 1.23 ± 0.05 mJy at 251 GHz.

the continuum flux density ratio $S_{\rm cont,[C\,II]}/S_{\rm cont,CO(6-5)} = 35 \pm 17$ for J0100+2802. Although $S_{\rm cont,[C\,II]}$ of many $z \gtrsim 6$ quasars are detected (e.g., Venemans et al. 2018), only six quasars were unambiguously detected (i.e., $>3\sigma$) for $S_{\rm cont,CO(6-5)}$ (Wang et al. 2010, 2011; Venemans et al. 2017b; Feruglio et al. 2018) in the literature to our knowledge. The $S_{\rm cont,[C\,II]}/S_{\rm cont,CO(6-5)}$ of these six quasars are in the range of 14.3–23.1, which is lower than that of J0100 +2802. This is consistent with our fitting, which suggests that the dust in the host galaxy of J0100+2802 has a high temperature and/or a larger dust emissivity index than the average values of other $z \gtrsim 6$ luminous quasars (e.g., Priddey & McMahon 2001; Beelen et al. 2006; Leipski et al. 2013). We note, however, that some $z \gtrsim 6$ quasars are not detected in the $S_{\rm cont,CO(6-5)}$ (e.g., Bertoldi et al. 2003; Wang et al. 2010), which means they could have $S_{\rm cont,[C\,II]}/S_{\rm cont,CO(6-5)} \gtrsim 30$, comparable to J0100+2802. Thus, we emphasize that future dust continuum observations at high frequency are needed to confirm whether the dust properties of J0100+2802 are different from those of other $z \gtrsim 6$ quasars.

3.2. FIR Luminosity and Dust Mass

In this subsection, we describe the effects on FIR luminosity, dust mass, and SFR measurements caused by the uncertainty of dust SED. We have to assume an SED shape of the dust emission in order to compute the FIR luminosity. In previous works, the dust SED was often assumed to be a thin graybody with $\beta = 1.6$ and $T_{\rm dust} = 47$ K (Beelen et al. 2006). With this assumption, we measured the FIR luminosity to be $L_{\rm FIR} = (3.5 \pm 0.7) \times 10^{12}\,L_\odot$, the dust mass to be $M_{\rm dust} = 2.0 \times 10^8\,M_\odot$, and the SFR to be $850\,M_\odot\,{\rm yr}^{-1}$ in Wang et al. (2016).

However, as shown above, the dust SED of J0100+2802 favors a warmer temperature and/or a higher emissivity index. Following Wang et al. (2016), we derive the FIR luminosity to be $L_{\rm FIR} = 7.8 \times 10^{12}\,L_\odot$ and total infrared luminosity of $L_{\rm TIR} = 1.3 \times 10^{13}\,L_\odot$ by integrating the graybody with $T_{\rm dust} = 47$ K and $\beta = 2.64$ from 42.5 μm to 122.5 μm and from 3 μm to 1100 μm, respectively. Applying a scaling relation between $L_{\rm TIR}$ and the SFR found in the local universe, $\log {\rm SFR}\,(M_\odot\,{\rm yr}^{-1}) = \log L_{\rm TIR}\,({\rm erg\,s}^{-1}) - 43.41$ (Kennicutt & Evans 2012), we find that the SFR in J0100+2802 is $1900\,M_\odot\,{\rm yr}^{-1}$. Previous studies of high-redshift starburst galaxies show that the dust emission could be optically thick at $\lambda_{\rm rest} \lesssim 200$ μm (e.g., Riechers et al. 2013), thus using continuum measurements at wavelength significantly longer than 200 μm are preferred to estimate the dust mass. Because the emission at $\lambda_{\rm rest} > 500$ μm of J0100+2802 could be affected by the nonthermal radio emission (see Figure 5), we thus use the CO (6–5) underlying continuum to estimate the dust mass. We follow the procedure described in Venemans et al. (2018) by assuming the dust opacity coefficient to be $\kappa_\nu(\beta) = 0.77\ (\nu/352\ {\rm GHz})^\beta\ {\rm cm^2\,g^{-1}}$. The dust mass estimated based on this dust temperature and emissivity index assumption is $M_{\rm dust} = 3.4 \times 10^7\,M_\odot$.

Assuming a graybody with $T_{\rm dust} = 60$ K and $\beta = 1.95$, we obtain $L_{\rm FIR} = 6.8 \times 10^{12}\,L_\odot$, $L_{\rm TIR} = 1.4 \times 10^{13}\,L_\odot$, ${\rm SFR} = 2060\,M_\odot\,{\rm yr}^{-1}$ and $M_{\rm dust} = 5.8 \times 10^7\,M_\odot$. When a higher dust temperature of 80 K and $\beta = 1.6$ is adopted, these values are $L_{\rm FIR} = 8.0 \times 10^{12}\,L_\odot$, $L_{\rm TIR} = 2.5 \times 10^{13}\,L_\odot$, ${\rm SFR} = 3760\,M_\odot\,{\rm yr}^{-1}$, and $M_{\rm dust} = 5.8 \times 10^7\,M_\odot$. The FIR luminosities and SFRs derived above are about 2–4 times higher and the dust masses are about 2–4 times lower than that derived by simply assuming $\beta = 1.6$ and $T_{\rm dust} = 47$ K.

As suggested by Clements et al. (2010), a steep dust SED can be explained with more than one dust component. In the discussion above, we assumed that the dust in J0100+2802 is heated mainly by star formation, which allows estimating the SFR based on the FIR luminosity. However, part of the dust emission in J0100+2802, the most intrinsically luminous object found at $z > 6$, might also be heated directly by the central power AGN. Our analysis on the gas excitation in the following section also supports this scenario, which will introduce additional uncertainties on estimating the SFR and dust mass in the host galaxy of J0100+2802. Therefore, we caution that the FIR luminosity, SFR, and dust mass measured here are still highly uncertain, and additional photometry at shorter wavelengths is needed to better constrain these parameters for the host galaxy of J0100+2802.

Table 2
Continuum Properties of J0100+2802

ν_{obs} (GHz)	ν_{rest} (GHz)	Flux Density (μJy)	Beam Size	Deconvolved Size	Deconvolved Size (kpc^2)
666[a]	4880	<30000	7.″9 × 7.″9	...	...
353[a]	2586	4100 ± 1200	13.″0 × 13.″0	...	...
258	1890	1470 ± 100	0.″24 × 0.″12	0.″46 × 0.″25	2.55 × 1.39
251	1839	1260 ± 80	0.″25 × 0.″13	0.″47 × 0.″27	2.61 × 1.50
244	1788	1110 ± 90	0.″26 × 0.″13	0.″48 × 0.″27	2.66 × 1.50
180	1319	362 ± 35	0.″60 × 0.″44	0.″40 × 0.″28	2.22 × 1.55
152	1114	178 ± 19	0.″76 × 0.″50	0.″52 × 0.″38	2.88 × 2.11
103	755	43 ± 12	0.″65 × 0.″47	...	...
99.4	728	36 ± 17	0.″24 × 0.″17	...	...
32[a]	234	14.8 ± 4.3	0.″74 × 0.″68	...	...
3[a]	22	104.5 ± 3.1	0.″65 × 0.″54	...	...
1.5[b]	11	91 ± 17	0.″012 ± 0.″005	0.″007 ± 0.″003	0.04 ± 0.02

Notes.
[a] Flux densities adopted from Wang et al. (2016).
[b] Adopted from Wang et al. (2017).

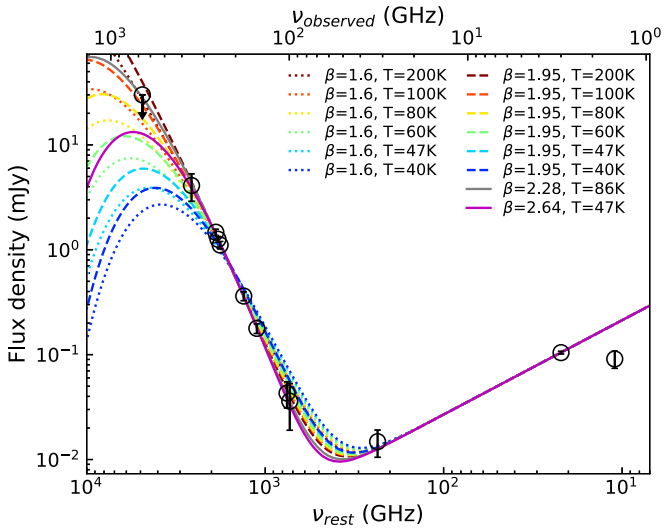

Figure 5. FIR dust continuum and radio emissions of the J0100+2802 host. The *Y*-axis shows the measured flux densities listed in Table 2, and the *x*-axis shows the observed (top) and rest-frame (bottom) frequencies. The dashed lines are graybody model fits with the emissivity index fixed at $\beta = 1.95$ (Priddey & McMahon 2001), and the dotted lines are models with fixed $\beta = 1.6$ (Beelen et al. 2006). The magenta solid line denotes a graybody model fit with T_{dust} fixed at 47 K. The gray solid line denotes a graybody model fit with both β and T_{dust} as free parameters, which yields $\beta = 2.28 \pm 0.26$ and $T_{dust} = 86 \pm 54$ K.

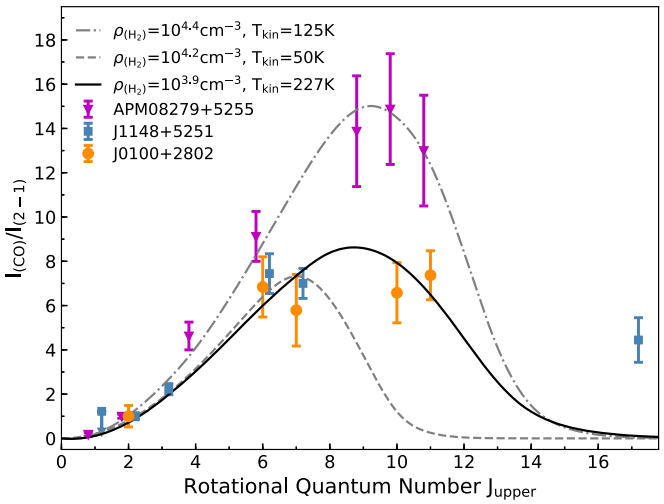

Figure 6. CO SLEDs of J0100+2802, J1148+5251, and APM 08279+5255. The orange circles denote the measured CO SLED of J0100+2802, the steel blue squares and magenta triangles denote the measured CO SLEDs of J1148+5251 and APM 08279+5255, respectively. The gray dashed line denotes the single LVG model fitting for J1148+5251 from Riechers et al. (2009), and the gray dash–dotted line denotes the single LVG model fitting for APM 08279+5255 from Weiß et al. (2007). The black solid curve represents the best-fit single LVG model for J0100+2802 with $n_{(H_2)} = 10^{3.9}$ cm^{-3} and $T_{kin} = 227$ K.

4. Gas Excitation

4.1. CO Spectral Line Energy Distribution

Low-*J* CO emissions provide crucial information on the cold molecular gas; on the other hand, high-*J* CO lines have critical densities $>10^5$ cm^{-3} and trace the warmer molecular gas in the center of galaxies. Thus the SLED of the CO emission lines can reveal the physical conditions, especially the gas temperature and density, of molecular gas (see Carilli & Walter 2013, for a review). One of the most detailed analysis examples is the highly excited gravitationally lensed quasar (APM 08279+5255) host galaxy at $z = 3.9$, investigated by Weiß et al. (2007). In this study, the authors found that APM 08279+5255 can be modeled with a single-component large velocity gradient (LVG) model with H_2 density of $n_{(H_2)} = 10^{4.4}$ cm^{-3} and a gas temperature of $T_{kin} = 125$ K. The fitting can be improved when both a cool gas component (∼65 K) powered by star formation and a warm (∼220 K) gas component directly heated by the central AGN are introduced. At higher redshifts (i.e., $z > 6$), the only CO SLED of quasar host galaxy that has been studied in detail is that of the quasar J1148+5251 at $z = 6.42$ (Riechers et al. 2009; Gallerani et al. 2014). Riechers et al. (2009) found that the CO SLED of J1148+5251 host galaxy can be best described by a single LVG model with $T_{kin} = 50$ K, and $n_{(H_2)} = 10^{4.2}$ cm^{-3}. Recently, Gallerani et al. (2014) claimed the detection of a very high-*J* CO (17–16) emission and suggested that the CO excitation might be explained by introducing a composite of photodissociation and X-ray-dominated region (PDRs and XDRs) models.

Because we have detected five CO lines, it is possible to diagnose the gas excitation in J0100+2802. The CO SLEDs of J0100+2802 and two examples mentioned above are shown in Figure 6. We normalize the CO SLEDs of each system by their CO (2–1) emissions for comparison. We use the 1D nonlocal thermal equilibrium (non-LTE) radiative transfer code,

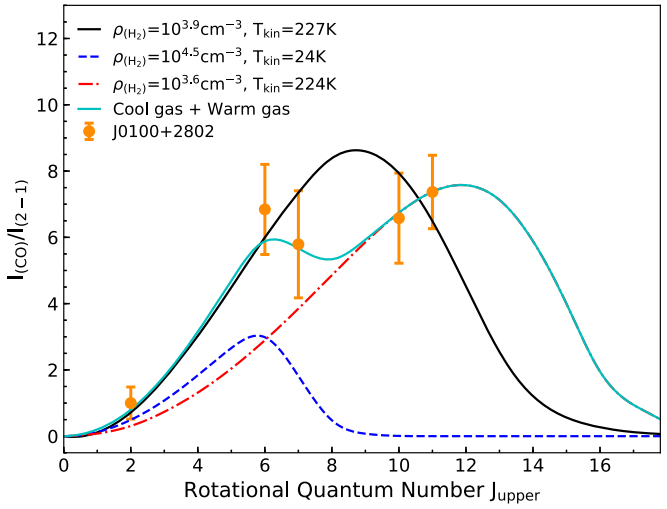

Figure 7. CO SLEDs of J0100+2802. The orange circles denote the measured CO SLED of J0100+2802. The black solid curve represents the best-fit single LVG model for J0100+2802 with $n_{(H_2)} = 10^{3.9}$ cm^{-3} and $T_{kin} = 227$ K. The blue dashed line and red dash–dotted lines represent the cool ($n_{(H_2)} = 10^{4.5}$ cm^{-3} and $T_{kin} = 24$ K) and hot ($n_{(H_2)} = 10^{3.6}$ cm^{-3} and $T_{kin} = 224$ K) gas component, respectively. The cyan solid line is the sum of the cool and hot gas components.

RADEX, that was developed by van der Tak et al. (2007) to study the CO excitation in the host galaxy of J0100+2802. The inputs of RADEX are the gas kinetic temperature (T_{kin}), the volume density of the molecular hydrogen ($n_{(H_2)}$), and the column density of the CO molecule (N_{CO}). We set the background temperature to be the CMB temperature at $z = 6.327$. We searched the minimum χ^2 within the parameter spaces of $n_{(H_2)} = 10^2$–10^7 cm^{-3}, $T_{kin} = T_{CMB}$–10^3 K, $N_{CO}/dv = 10^{15.5}$–$10^{19.5}$ cm^{-2} (km s^{-1})$^{-1}$ (Yang et al. 2017). The minimum reduced χ^2 ($\chi_{red}{}^2 = 2$) yields $T_{kin} = 227$ K, $n_{(H_2)} = 10^{3.9}$ cm^{-3} for a single LVG model. The best-fit model is shown as the black solid line in Figure 6; the best-fit single LVG model does not reproduce the shape of CO SLED well, suggesting that the CO excitation in J0100+2802 is more complicated (i.e., needs two or more gas components).

Similar to Weiß et al. (2007) and Yang et al. (2017), we split the CO SLED into two components in the RADEX modeling. We adopt the same parameter space as we used for single LVG model fitting. Instead of using χ^2 fitting, we performed Markov chain Monte Carlo (Foreman-Mackey et al. 2013) calculations to fit our observed fluxes with the fluxes generated from RADEX models following the procedure explored by Yang et al. (2017). The best-fit model is shown in Figure 7. The median value and $\pm1\sigma$ range of the values from the probability distribution are found to be $n_{(H_2)} = 10^{4.5^{+1.1}_{-1.1}}$ cm^{-3} and $T_{kin} = 24^{+8}_{-3}$ K for the cool component and $n_{(H_2)} = 10^{3.60^{+1.3}_{-0.8}}$ cm^{-3} and $T_{kin} = 224^{+165}_{-100}$ K for the warm component.

We measure that $L_{CO(10-9)}/L_{CO(6-5)} = 1.60 \pm 0.28$ and $L_{CO(11-10)}/L_{CO(6-5)} = 1.98 \pm 0.24$ in J0100+2802, which is much higher than that of most starburst galaxies (see Figure 6 in Carniani et al. 2019). This suggests that the central AGN in J0100+2802 could directly heat the molecular gas in the quasar host galaxy, especially considering that J0100+2802 is the most luminous AGN that hosts the most massive SMBH known at $z > 6$. However, we note that there are some dusty starburst galaxies in the early universe that are not known to host luminous AGNs, which also show comparable bright high-J CO emissions that might be produced by cooler gas components with higher density (e.g., Riechers et al. 2013; Yang et al. 2017). Thus, future ALMA observations of higher-J CO lines (i.e., $J_{upp} > 13$) are needed to distinguish whether the bright high-J CO emissions are excited by powerful AGN or from cooler gas with higher density.

4.2. Molecular Gas Mass

For high-redshift FIR luminous objects, a luminosity-to-mass conversion factor of $\alpha_{CO} = 0.8\,M_\odot$ (K km s^{-1} pc^2)$^{-1}$, derived from moderate-density warm inter-cloud medium, is usually adopted (Downes & Solomon 1998) when the H_2 mass is calculated from CO observations. For J0100+2802, the H_2 density derived for cool and hot gas components is $n_{(H_2)} \sim 10^{4.5}$ cm^{-3} and $n_{(H_2)} \sim 10^{3.6}$ cm^{-3}, respectively. This is comparable with that of ULIRGS, which is $n_{(H_2)} \sim 10^{4.0}$ cm^{-3}. The temperature of the warm gas components is about five times higher than that in ULIRGS, however. The conversion factor α_{CO} scales as $n^{0.5}_{(H_2)}/T_{kin}$ (Weiß et al. 2007). This suggests that the conversion factor for the warm gas component could be $\alpha_{CO} \sim 0.16\,M_\odot$ (K km s^{-1} pc^2)$^{-1}$. The CO(1–0) line fluxes estimated for cool and warm gas based on the best-fit two-component LVG model are 6.0×10^9 K km s^{-1} pc^2 and 3.7×10^9 K km s^{-1} pc^2, respectively. Thus, we estimate the molecular gas mass to be $M_{cool} = (4.8 \pm 1.6) \times 10^9\,M_\odot$, and $M_{warm} = (5.9 \pm 0.8) \times 10^8\,M_\odot$ by assuming $\alpha_{CO} = 0.8\,M_\odot$ (K km s^{-1} pc^2)$^{-1}$ for the cool gas and $\alpha_{CO} = 0.16\,M_\odot$ (K km s^{-1} pc^2)$^{-1}$for the warm gas, respectively. The total molecular gas mass is $M_{H_2} = (5.4 \pm 1.6) \times 10^9\,M_\odot$. The gas mass measured here is about twice lower than that measured by Wang et al. (2016) because Wang et al. (2016) adopted $\alpha_{CO} = 0.8\,M_\odot$ (K km s^{-1} pc^2)$^{-1}$ for the total CO(1–0) flux and assumed that $L'_{CO(1-0)} = L'_{CO(2-1)}$. Because the CO SLED model of J0100+2802 is still highly uncertain and the measurable line luminosities from the cool component could be affected by the CMB, which has a similar temperature as that of the cool component, the estimated gas mass still has large uncertainties.

On the other hand, the gas mass can also be estimated from the dust mass (e.g., Draine et al. 2007). From our dust SED models, we derive a dust mass of $M_{dust} = 3.4 \times 10^7\,M_\odot$ for $T_{dust} = 47$ K and $\beta = 2.64$, $M_{dust} = 5.8 \times 10^7\,M_\odot$ for $T_{dust} = 60$ K and $\beta = 1.95$ and $M_{dust} = 5.8 \times 10^7\,M_\odot$ for $T_{dust} = 80$ K and $\beta = 1.6$. Assuming a gas-to-dust mass ratio of 80 (e.g., Riechers et al. 2013), we obtain a gas mass of $M_{H_2} = 2.7 \times 10^9$–$4.6 \times 10^9\,M_\odot$. This gas mass is similar to the one we estimated from the LVG model. Adopting the gas mass measured from the LVG model and the SFR from dust SED fitting, we can derive the molecular gas depletion timescale: $t_{dep}(H_2) = \frac{M_{H_2}}{SFR}$. By considering all the three different dust SEDs we explored in Section 3.1, we estimate that the molecular gas depletion timescale in the host galaxy of J0100+2802 is only about 10^6 yr. However, given the high luminosity of the quasar, it is possible that some fraction of the dust is heated by the central AGN directly, as discussed in Section 3.1, in which case the gas depletion timescale quoted above becomes a lower limit.

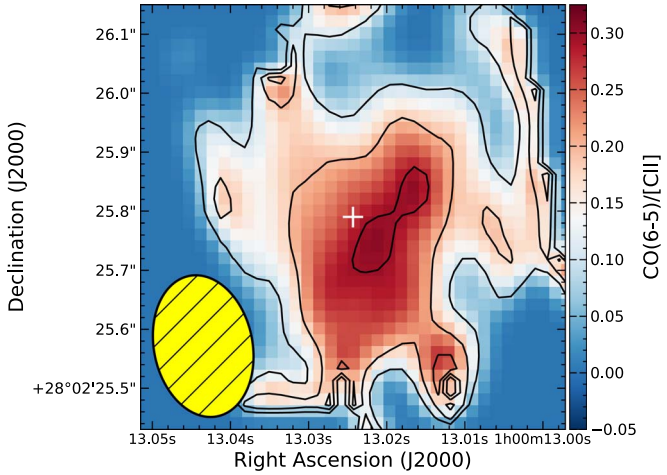

Figure 8. The CO(6–5) and [C II] line emission intensity map ratio within the central region ($r = 0\farcs4$ or 2.2 kpc). The resolution for the [C II] intensity map is downgraded to be the same with that of CO(6–5). Both lines are integrated from -300 to $+300$ km s^{-1}. The beam is shown in the lower left corner as a cyan ellipse. The contours indicate the 0.1, 0.2, and 0.3 isophotes. The intensity ratio map suggests that dense molecular gas is more centrally concentrated than the [C II] emission. The large ratio region at the edge of this map may not be reliable considering that both the [C II] and CO(6–5) intensities in these region are lower than 3σ.

4.3. Line Ratios

In order to give a first-order constraint on the spatially resolved excitation, we downgrade the resolution of the [C II] intensity map to be exactly the same with that of CO(6–5) emission. The intensity map ratio is shown in Figure 8. The intensity maps of both CO(6–5) and [C II] are integrated from -300 km s^{-1} to $+300$ km s^{-1}. The CO(6–5)/[C II] ratio decreases from ~0.3 to ~0.1 from the galaxy center to regions out to ~1 kpc, indicating that (1) the CO(6–5) is more centrally concentrated than [C II], (2) the overall gas density is $n \gtrsim 10^{4.5}$ cm^{-3}, unless the radiation field intensity is lower than 1000 G_0 for a classic PDR model (Kaufman et al. 1999, 2006; Pound & Wolfire 2008), and (3) the gas density and/or the radiation field are higher in the most central region than that at $\gtrsim$1 kpc. We also measure the [C II]/[C I] ratio to be $\gtrsim$47, corresponding to a radiation field higher than $10^{3.5}$ G_0 for $n \sim 10^5$ cm^{-3}. All these line ratios suggest that both the gas density and the radiation field in the host galaxy of J0100+2802 are relatively high ($n \sim 10^5$ cm^{-3} and radiation field $>10^3$ G_0). The line luminosity ratio of [C II] and [C I] in J0100+2802 is significantly higher than the maximum line ratio predicted for XDR models of Meijerink et al. (2007). Similar results are also found in other $z > 6$ quasars (e.g., Venemans et al. 2017b). This suggests that the atomic gas traced by [C II] and [C I] is dominated by the PDRs. Future high spatial resolution observations on multiple lines are necessary to further explore the spatially resolved excitation in the host galaxy of J0100+2802.

5. Gas Kinematics and Dynamical Mass

5.1. Gas Kinematics

The coincidence of the positions of the blue and red sides of the CO(6–5) and [C II] emission lines suggests that neither atomic nor molecular have ordered motions on kiloparsec scales. In order to further study the kinematics of the gas in the host galaxy of J0100+2802, we examine the velocity channel map of the [C II] line in Figure 9 and that of the CO(6–5) line in Figure 10. The peak positions of the [C II] and CO(6–5) emissions in the individual velocity channels are fully consistent with the *GAIA* position, indicating that there is no clear rotation in the host galaxy of J0100+2802 on scales of ~1 kpc. Similar gas kinematics is also seen in other high-redshift quasar host galaxies (e.g., Walter et al. 2009; Venemans et al. 2017a) and in brightest cluster galaxies (BCGs; e.g., McNamara et al. 2014; Werner et al. 2014).

If the [C II] and CO(6–5) structures are rotationally supported, their rotation axes must be very close to our line of sight (i.e., nearly face-on). The axial ratios derived from [C II] and CO(6–5) are $b/a = 0.8 \pm 0.35$ and $b/a = 0.74 \pm 0.67$, respectively. This could be consistent with a nearly face-on morphology, although with large uncertainties. However, as shown in Section 2, there could be additional extended emissions beyond our current detection limits, thus there could still be rotational components at larger scales.

Figure 9 suggests that there are some individual clumps in several velocity channels, but the sizes of these clumps are comparable to the beam size, and the signal-to-noise ratios for these individual clump detections are relative low (i.e., peaks at ~5σ). Future deeper and higher resolution ALMA observations will allow us to reveal whether the host galaxy of J0100+2802 is clumpy or traced by mergers.

5.2. Dynamical Mass

The dynamical mass of high-redshift quasar host galaxy is usually estimated by assuming that the line stems from a rotating disk. In Wang et al. (2016), we measured the dynamical mass of J0100+2802 based on this method by assuming the diameter of the rotating gas disk to be $D = 4.5 \pm 1.5$ kpc, the typical FWHM major axis sizes of [C II] emission from $z \sim 6$ quasar hosts (e.g., Wang et al. 2013). We had to make this assumption because we were not able to resolve the [C II] emission from our PdBI observations (Wang et al. 2016).

In Section 2.3 we measured the radius of the quasar host galaxy to be $R_{\rm major} = 3.6 \pm 0.2$ kpc and the FWHM of [C II] emission to be 380 ± 16 km s^{-1}. If the [C II] line stems from a rotating gas disk and the circular velocity can be estimated as $v_{\rm cir} = 0.75 \times {\rm FWHM}_{\rm [C\,II]}/\sin(i)$, where i is the inclination angle ($i = 0$ means face-on), the dynamical mass can then be estimated as $M_{\rm dyn} = 1.16 \times 10^5\, v_{\rm cir}^2\, D = (7.0 \pm 1.3) \times 10^{10}/\sin^2(i)\, M_\odot$. The axis ratio of [C II] map is $b/a = 0.8 \pm 0.35$, corresponding to $i \sim 37°$. This yields a dynamical mass of $\sim 1.9 \times 10^{11}\, M_\odot$, an order of magnitude lower than estimated based on the mass ratio of SMBHs and bulges in local elliptical galaxies (e.g., Equation (10) in Kormendy & Ho 2013). However, because we do not see any velocity gradient in the [C II] emission and the inclination angle has a large uncertainty, it is likely that the gas is not supported by rotation, or that the disk is observed nearly face-on (i.e., $i \sim 0°$). If we assumed $i = 5°$, we would derive a dynamical mass of $\sim 8.9 \times 10^{12}\, M_\odot$, comparable to the mass estimated from the local relation.

If the gas is dynamically hot and supported by random motion, we can estimate the dynamical mass using the virial theorem following Venemans et al. (2017a). The velocity dispersion is measured to be 161 ± 7 km s^{-1} from the tapered spectrum shown in Figure 1. The M–σ relation of both $z > 6$ quasars and local early-type galaxies is shown in Figure 11.

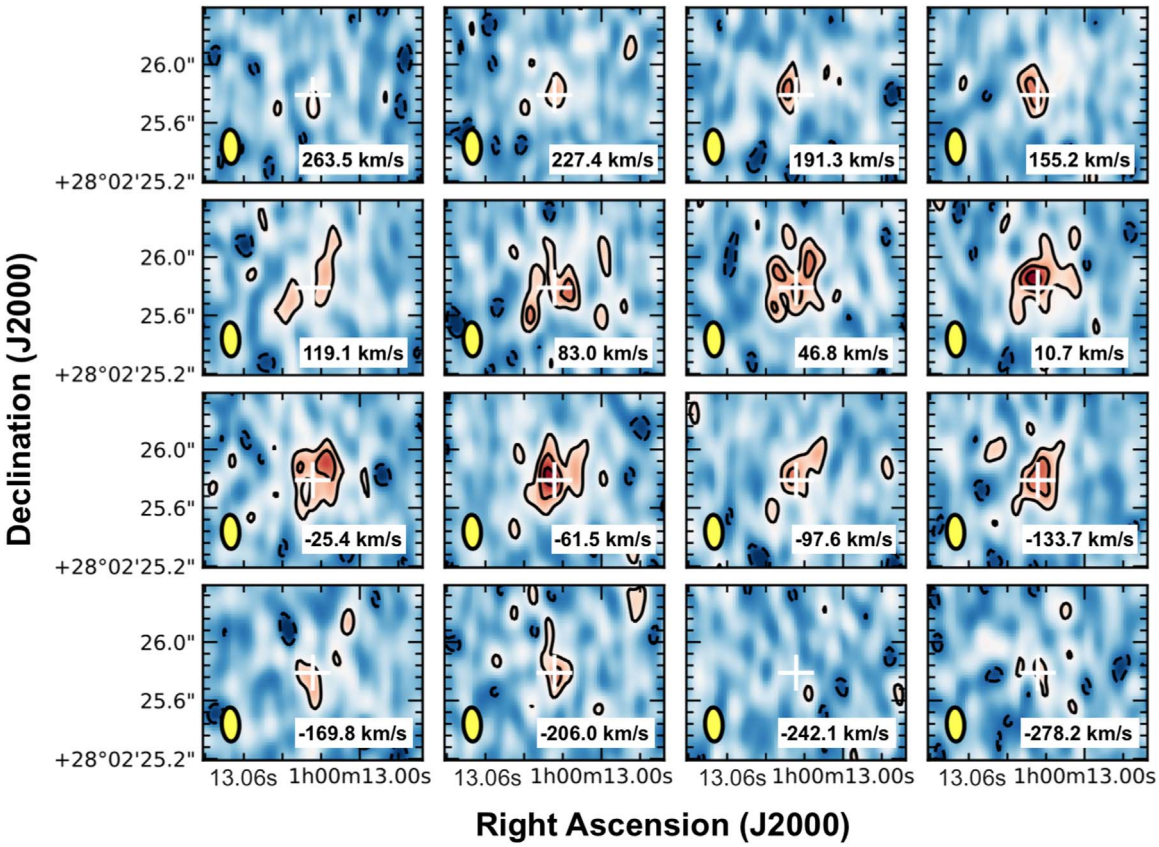

Figure 9. [C II] emission channel map. The velocity resolution is ∼36 km s^{-1}. The [C II] emission is clearly detected in more than 10 channels. Solid contour levels are +3, +5, and +7σ, where $\sigma = 0.21$ mJy/beam. The −2σ contours are presented by dashed lines.

Clearly, J0100+2802, as well as many other luminous high-redshift quasars, does not following the $M_{\rm BH}$–σ relation derived from local galaxies. The dynamical mass is measured to be $M_{\rm dyn} = 3R\sigma^2/2G = (3.25 \pm 0.46) \times 10^{10}\,M_\odot$, which is comparable to that of other $z \sim 6$ quasar host galaxies (e.g., Walter et al. 2009; Wang et al. 2013; Willott et al. 2015; Venemans et al. 2016, 2017a, 2017c). Intriguingly, the SMBH measured from the single-epoch virial method based on the Mg II line is $1.24 \times 10^{10} M_\odot$ (Wu et al. 2015), which is 38% of the dynamical mass measured here. This could imply that J0100+2802 has the largest SMBH and highest dynamical mass ratio in all known $z \gtrsim 6$ quasars; the next highest value (J1148+5251) is ∼25% (Walter et al. 2009; Willott et al. 2015). Even considering the large uncertainty on the SMBH mass measurement, which could be up to 0.5 dex (Shen 2013), the SMBH and dynamical mass ratio in J0100+2802 is still more than one order of magnitude higher than that in the local elliptical galaxies (e.g., Kormendy & Ho 2013).

5.3. Mass Budgets

The BH mass in J0100+2802 is measured to be $M_{\rm BH} = (1.24 \pm 0.19) \times 10^{10}\,M_\odot$ (Wu et al. 2015). The molecular gas mass measured from the two-component LVG model in Section 4.2 is $M_{\rm H_2} = 5.4 \times 10^9\,M_\odot$. We choose a fiducial dust SED of $T_{\rm dust} = 60$ K and $\beta = 1.95$, which gives a dust mass of $M_{\rm dust} = 5.9 \times 10^7\,M_\odot$. The atomic gas mass measured from the [C II] emission is $M_{\rm atomic} \sim 3 \times 10^9\,M_\odot$ (Wang et al. 2016). All these mass measurements together lead to a first-order constraint on the stellar mass in the host galaxy of J0100+2802. By assuming that dark matter does not significantly contribute to the mass budget (e.g., Genzel et al. 2017), we can give an upper limit of the stellar mass of $M_* < 1.2 \times 10^{10}\,M_\odot$ using the virial theorem measured dynamical mass. If we were to use the dynamical mass measured from a face-on disk, however, the quasar host galaxy would contain a high stellar mass on the order of 10^{11}–$10^{12}\,M_\odot$, which is at the high end of the stellar mass function derived for star-forming galaxies at similar redshifts (e.g., Bowler et al. 2014). The high stellar mass scenario is also supported by the presence of radio emission in J0100+2802 (Wang et al. 2017), because galaxies with a higher stellar mass tend to have higher radio activity (e.g., Best et al. 2005). However, due to the large uncertainties in the derived dynamical mass, we cannot place tight constraints on the stellar mass in the host galaxy of J0100+2802.

From another perspective, when we assume that the velocity dispersion measured from [C II] does represent the dynamics of the quasar host galaxy, we can use the velocity dispersion measured from the [C II] emission line and the Mg II based BH mass to estimate the radius of the sphere of influence of the central BH: $r_{\rm soi} = \frac{GM_{\rm BH}}{\sigma_*^2} \sim 2$ kpc, which is more than twice higher than our beam size and comparable with the size of the [C II] emission region. This suggests that the kinematic of the [C II] emission is strongly affected by the potential of the central SMBH. This requires a reexamination of the mass budget discussed above. In this case, the mass estimated using the virial theorem can be interpreted as the upper limit of the BH mass if the [C II] emission dynamics is dominated by the SMBH potential. On the other hand, if the host galaxy of J0100+2802 is a nearly face-on rotating disk, as discussed above, the

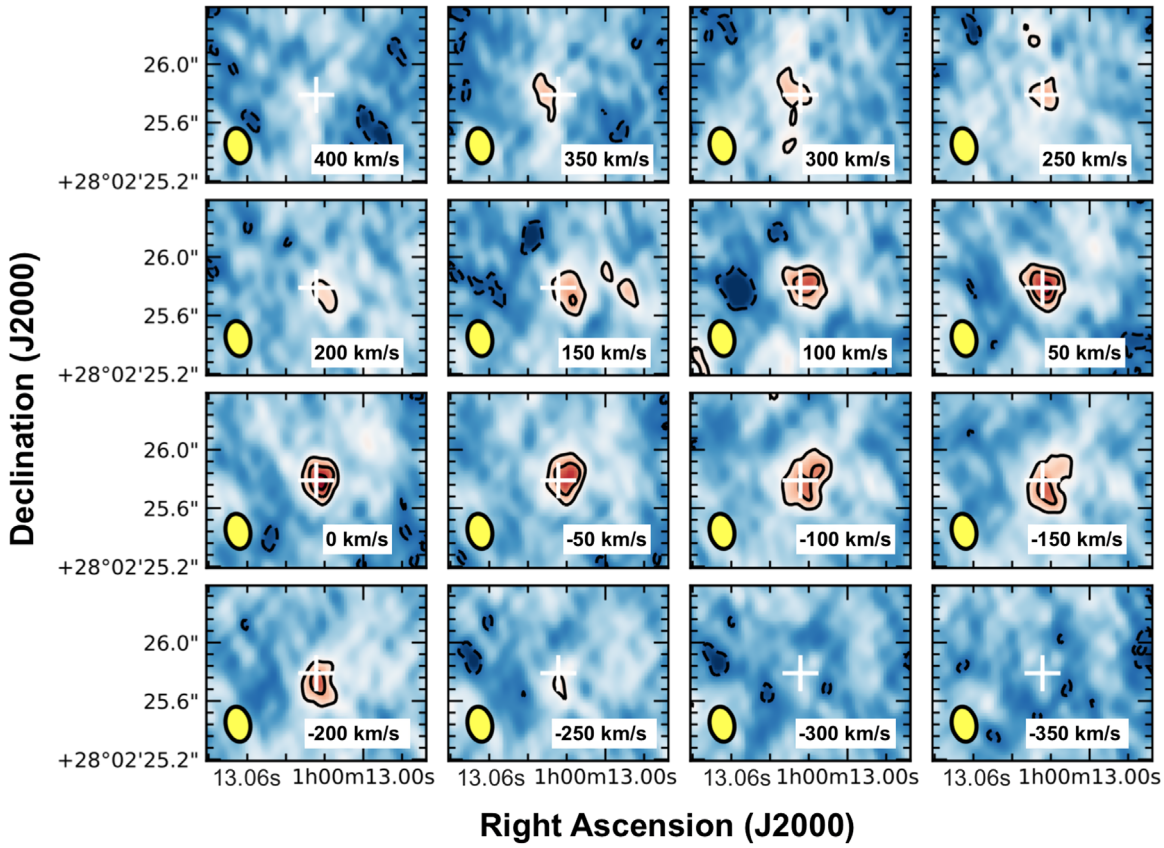

Figure 10. CO(6–5) emission channel map. The velocity resolution is 50 km s^{-1}. The CO(6–5) is clearly detected in more than 10 channels. Solid contour levels are $+3$, $+5$, and $+7\sigma$, where $\sigma = 0.058$ mJy/beam. The -2σ contours are presented by dashed lines.

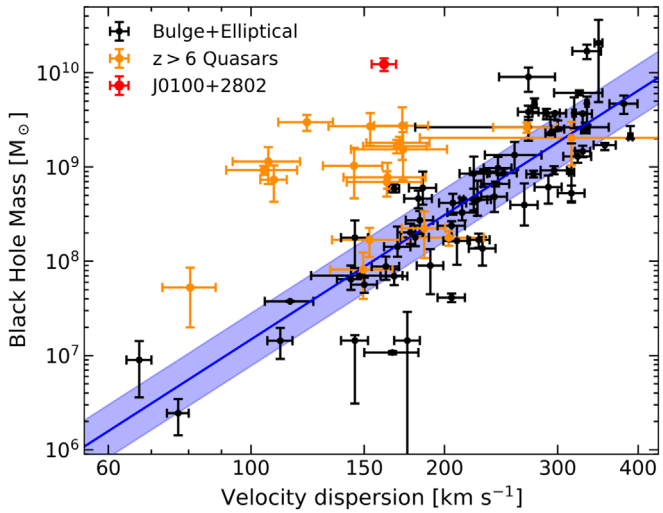

Figure 11. The $M_{\rm BH}$–σ relation. The large red circle denotes J0100+2802. The orange circles are other $z \gtrsim 6$ quasars with both Mg II based on single-epoch virial BH mass measurements and [C II] line observations. The BH masses are compiled by Wang et al. (2015), and the [C II] line widths are from the compilation by Decarli et al. (2018). The small black circles are local elliptical galaxies or galaxies with classical bulges, collected by Kormendy & Ho (2013). The blue solid line and shaded region denote the best-fit $M_{\rm BH}$–σ relation in local galaxies (Kormendy & Ho 2013). The systematic uncertainty of the single-epoch virial BH mass measurement, which could be up to 0.5 dex (Shen 2013), is not include in the plot.

BH mass and dynamical mass could still follow the local relation (e.g., Kormendy & Ho 2013). In this case, we can roughly estimate the radius of the sphere of influence of the central BH with the Mg II based BH mass and the local $M_{\rm BH}$–σ relation, which yields $r_{\rm soi} \sim 250$ pc. The sphere of influence is smaller than our beam size, but it is still much larger than that of other high-redshift quasars and can be resolved by future higher resolution ALMA observations. This will allow us to dynamically measure the BH mass at the end of reionization.

Moreover, we note that the [C II] and CO(6–5) traced gas could be gravitationally unbounded, in which case the dynamical mass of the quasar host galaxy might be significantly different from the value quoted here. Although we do not see any obvious merger signatures in our current data, we cannot rule out a late-stage merger that is beyond the sensitivity of current observations. We also seem to miss some faint extended emissions, and we cannot rule out minor mergers either, which are traced by faint galaxies at the outskirts of the quasar host galaxy.

In summary, we find that while the narrow [C II] and CO line width in the J0100+2802 host is suggestive of a modest dynamical mass compared to the prediction from the local $M_{\rm BH}$ versus $M_{\rm dyn}$ relation, observations with considerably higher signal-to-noise ratio and spatial resolution are needed to build a full dynamical model by including the influence of BH gravity, pressure support from gas random motion, the possibility of a nearly face-on morphology, or the presence of merger activity.

6. Summary

In this work, we presented multi-band ALMA observations of the dust continuum and the [C II] emission and CO emission lines in the host galaxy of J0100+2802. Dust continuum and the [C II] and CO(6–5) emission are spatially resolved at the

subkiloparsec scale. We also detected high-J CO lines in CO(11–10), CO(10–9), and CO(7–6). The main findings of this work are listed below.

1. We model the dust continuum SED over a wide frequency coverage and find that the dust in J0100+2802 either has a high dust emissivity $\beta \gtrsim 2$ or a high dust temperature $T_{\rm dust} \gtrsim 60$ K, or a combination of these two factors. This distinguishes J0100+2802 from other $z > 6$ quasars, most of which have lower dust temperatures. The FIR luminosity and SFR derived from several allowed dust SED models with warm temperature and/or high dust emissivity are about 2–4 times higher and the dust mass is about 2–4 times lower than that derived by simply assuming $\beta = 1.6$ and $T_{\rm dust} = 47$ K.
2. We model the CO SLED of J0100+2802 with the LVG method. The CO SLED can be explained by a two-component gas model, a cool component at ~24 K with a high density of $n_{(\rm H_2)} = 10^{4.5}\,\rm cm^{-3}$, and a warm component at ~224 K with a slightly lower density of $n_{(\rm H_2)} = 10^{3.6}\,\rm cm^{-3}$. The total molecular gas mass is measured to be $M_{\rm H_2} = 5.4 \times 10^9\,M_\odot$ based on the LVG model. The high $L_{\rm CO(10-9)}/L_{\rm CO(6-5)}$ and $L_{\rm CO(11-10)}/L_{\rm CO(6-5)}$ ratios suggest that the central powerful AGN in J0100+2802 could directly heat the gas in the quasar host galaxy, but future ALMA observations of higher-J CO lines (i.e., $J_{\rm upp} > 13$) are needed to determine whether the bright high-J CO emissions are excited by powerful AGN or by cooler gas with higher density.
3. We also investigate the spatial distribution of the [C II] and CO(6–5) line ratios in the host galaxy of J0100+2802. This distribution indicates that the molecular gas traced by the CO(6–5) emission lives in a more central concentrated dense region than the [C II] emission. With the bright [C II] emission, the nondetection of [C I] emission indicates that the atomic gas in the host galaxy of J0100+2802 is dominated by the PDRs.
4. We examine the kinematics of J0100+2802 using spatially resolved [C II] and CO(6–5) observations, and find no ordered motion on kiloparsec scales. The velocity dispersion measured from the [C II] emission line is about three times smaller than that expected from the local $M_{\rm BH}$–σ relation. The dynamical mass of J0100+2802 measured using the virial theorem is only three times higher than the central BH. However, our current observations cannot rule out that the galaxy is a face-on disk galaxy, which still allow sthe dynamical mass of J0100+2802 following the local $M_{\rm BH}$ and $M_{\rm dyn}$ relation.

J0100+2802 is the most luminous object found at the end of reionization, and the central BH mass is measured to be $1.24 \times 10^{10}\,M_\odot$ using the single-epoch virial method. The gravitational radius of influence of the BH in J0100+2802 can be resolved with future considerably higher signal-to-noise ratio and spatial resolution ALMA observations, which will allow us to dynamically measure the BH mass. The notable highly excited molecular gas and warm dust temperature suggest that future deep ALMA observations on multiple emission lines and dust continuum are valuable for investigating the AGN feedback on the formation of the early massive galaxy.

F.W., X.-B.W., and R.W. acknowledge support from the National Key R&D Program of China (2016YFA0400703) and the National Science Foundation of China (11533001 & 11721303). X.F., J.Y., and M.Y. acknowledge support from the US NSF grant AST-1515115 and NASA ADAP grant NNX17AF28G. R.W. acknowledges support from the National Science Foundation of China grant No. 11473004. F.W. thanks the ENIGMA group members at UCSB for valuable comments on this work. We thank the anonymous referee for carefully reading the manuscript and providing constructive comments and suggestions to improve the manuscript.

The National Radio Astronomy Observatory is a facility of the National Science Foundation operated under cooperative agreement by Associated Universities, Inc. This paper makes use of the following ALMA data: ADS/JAO.ALMA#2015.1.00692.S and ADS/JAO.ALMA#2017.1.00624.S. ALMA is a partnership of ESO (representing its member states), NSF (USA) and NINS (Japan), together with NRC (Canada), MOST and ASIAA (Taiwan), and KASI (Republic of Korea), in cooperation with the Republic of Chile. The Joint ALMA Observatory is operated by ESO, AUI/NRAO and NAOJ. This paper also used the data based on observations under projects VLA/14B-151 and VLA/15A-494 with the VLA, and project M15BI055 with JCMT/SCUBA-2.

Facilities: ALMA, VLA, JCMT (SCUBA-2).

ORCID iDs

Feige Wang https://orcid.org/0000-0002-7633-431X
Xiaohui Fan https://orcid.org/0000-0003-3310-0131
Xue-Bing Wu https://orcid.org/0000-0002-7350-6913
Jinyi Yang https://orcid.org/0000-0001-5287-4242
Roberto Neri https://orcid.org/0000-0002-7176-4046
Minghao Yue https://orcid.org/0000-0002-5367-8021

References

Bañados, E., Venemans, B. P., Decarli, R., et al. 2016, ApJS, 227, 11
Bañados, E., Venemans, B. P., Mazzucchelli, C., et al. 2018, Natur, 553, 473
Beelen, A., Cox, P., Benford, D. J., et al. 2006, ApJ, 642, 694
Bertoldi, F., Cox, P., Neri, R., et al. 2003, A&A, 409, L47
Best, P. N., Kauffmann, G., Heckman, T. M., et al. 2005, MNRAS, 362, 25
Bowler, R. A. A., Dunlop, J. S., McLure, R. J., et al. 2014, MNRAS, 440, 2810
Carilli, C. L., & Walter, F. 2013, ARA&A, 51, 105
Carniani, S., Gallerani, S., Vallini, L., et al. 2019, arXiv:1902.01413
Clements, D. L., Dunne, L., & Eales, S. 2010, MNRAS, 403, 274
Condon, J. J. 1997, PASP, 109, 166
da Cunha, E., Groves, B., Walter, F., et al. 2013, ApJ, 766, 13
Decarli, R., Walter, F., Venemans, B. P., et al. 2018, ApJ, 854, 97
Downes, D., & Solomon, P. M. 1998, ApJ, 507, 615
Draine, B. T., & Lee, H. M. 1984, ApJ, 285, 89
Draine, B. T., Dale, D. A., Bendo, G., et al. 2007, ApJ, 663, 866
Fan, X., Narayanan, V. K., Lupton, R. H., et al. 2001, AJ, 122, 2833
Feruglio, C., Fiore, F., Carniani, S., et al. 2018, A&A, 619, A39
Foreman-Mackey, D., Hogg, D. W., Lang, D., & Goodman, J. 2013, PASP, 125, 306
Gallerani, S., Fan, X., Maiolino, R., & Pacucci, F. 2017, PASA, 34, e022
Gallerani, S., Ferrara, A., Neri, R., & Maiolino, R. 2014, MNRAS, 445, 2848
Genzel, R., Schreiber, N. M. F., Übler, H., et al. 2017, Natur, 543, 397
Hodge, J. A., Swinbank, A. M., Simpson, J. M., et al. 2016, ApJ, 833, 103
Ikarashi, S., Ivison, R. J., Caputi, K. I., et al. 2015, ApJ, 810, 133
Jiang, L., Fan, X., Annis, J., et al. 2008, AJ, 135, 1057
Jiang, L., Fan, X., Vestergaard, M., et al. 2007, AJ, 134, 1150
Kaufman, M. J., Wolfire, M. G., Hollenbach, D. J., & Luhman, M. L. 1999, ApJ, 527, 795
Kaufman, M. J., Wolfire, M. G., & Hollenbach, D. J. 2006, ApJ, 644, 283
Kennicutt, R. C., & Evans, N. J. 2012, ARA&A, 50, 531
Kormendy, J., & Ho, L. C. 2013, ARA&A, 51, 511

Leipski, C., Meisenheimer, K., Walter, F., et al. 2013, ApJ, 772, 103
Matsuoka, Y., Onoue, M., Kashikawa, N., et al. 2018, PASJ, 70, S35
McMullin, J. P., Waters, B., Schiebel, D., Young, W., & Golap, K. 2007, adass XVI, 376, 127
McNamara, B. R., Russell, H. R., Nulsen, P. E. J., et al. 2014, ApJ, 785, 44
Mechtley, M., Windhorst, R. A., Ryan, R. E., et al. 2012, ApJL, 756, L38
Meijerink, R., Spaans, M., & Israel, F. P. 2007, A&A, 461, 793
Mortlock, D. J., Warren, S. J., Venemans, B. P., et al. 2011, Natur, 474, 616
Pacucci, F., Volonteri, M., & Ferrara, A. 2015, MNRAS, 452, 1922
Pound, M. W., & Wolfire, M. G. 2008, adass XVII, 394, 654
Priddey, R. S., & McMahon, R. G. 2001, MNRAS, 324, L17
Riechers, D. A., Walter, F., Bertoldi, F., et al. 2009, ApJ, 703, 1338
Riechers, D. A., Bradford, C. M., Clements, D. L., et al. 2013, Natur, 496, 329
Shen, Y. 2013, BASI, 41, 61
Shen, Y., Wu, J., Jiang, L., et al. 2019, ApJ, 873, 35
van der Tak, F. F. S., Black, J. H., Schöier, F. L., Jansen, D. J., & van Dishoeck, E. F. 2007, A&A, 468, 627
Venemans, B. P., Decarli, R., Walter, F., et al. 2018, ApJ, 866, 159
Venemans, B. P., Walter, F., Decarli, R., et al. 2017a, ApJ, 837, 146
Venemans, B. P., Walter, F., Decarli, R., et al. 2017b, ApJ, 845, 154
Venemans, B. P., Walter, F., Decarli, R., et al. 2017c, ApJL, 851, L8
Venemans, B. P., Walter, F., Zschaechner, L., et al. 2016, ApJ, 816, 37
Walter, F., Riechers, D., Cox, P., et al. 2009, Natur, 457, 699
Wang, F., Fan, X., Yang, J., et al. 2017, ApJ, 839, 27
Wang, F., Wu, X.-B., Fan, X., et al. 2015, ApJL, 807, L9
Wang, F., Wu, X.-B., Fan, X., et al. 2016, ApJ, 819, 24
Wang, F., Yang, J., Fan, X., et al. 2018a, ApJL, 869, L9
Wang, F., Yang, J., Fan, X., et al. 2018b, arXiv:1810.11926
Wang, R., Carilli, C. L., Neri, R., et al. 2010, ApJ, 714, 699
Wang, R., Wagg, J., Carilli, C. L., et al. 2011, AJ, 142, 101
Wang, R., Wagg, J., Carilli, C. L., et al. 2013, ApJ, 773, 44
Wang, R., Wu, X.-B., Neri, R., et al. 2016, ApJ, 830, 53
Wang, R., Momjian, E., Carilli, C. L., et al. 2017, ApJL, 835, L20
Weiß, A., Downes, D., Neri, R., et al. 2007, A&A, 467, 955
Werner, N., Oonk, J. B. R., Sun, M., et al. 2014, MNRAS, 439, 2291
Willott, C. J., Bergeron, J., & Omont, A. 2015, ApJ, 801, 123
Willott, C. J., Delorme, P., Reylé, C., et al. 2010, AJ, 139, 906
Wu, X.-B., Wang, F., Fan, X., et al. 2015, Natur, 518, 512
Yang, C., Omont, A., Beelen, A., et al. 2017, A&A, 608, A144
Yang, J., Wang, F., Fan, X., et al. 2019, AJ, 157, 236